bioRxiv preprint doi: https://doi.org/10.1101/2025.11.20.689588; this version posted November 21, 2025. The copyright holder for this preprint (which was not certified by peer review) is the author/funder. All rights reserved. No reuse allowed without permission.

The fMRI response to transcranial photobiomodulation: the effect of wavelength, irradiance, frequency and skin tone on the BOLD and CBF response in healthy young adults

Hannah Van Lankveld[1,2], Joanna X. Chen[1,2], Xiaole Z. Zhong[1,3] and J. Jean Chen[1,2,3]

[1] Rotman Research Institute, Baycrest, Toronto, ON, Canada

[2] Biomedical Engineering, University of Toronto, Toronto, ON, Canada

[3] Medical Biophysics, University of Toronto, Toronto, ON, Canada

bioRxiv preprint doi: https://doi.org/10.1101/2025.11.20.689588; this version posted November 21, 2025. The copyright holder for this preprint (which was not certified by peer review) is the author/funder. All rights reserved. No reuse allowed without permission.

Abstract

Transcranial photobiomodulation (tPBM) is an emerging technology that utilizes light to penetrate the skull to stimulate neural tissue. However, the physiological impact and the in vivo dose dependence of tPBM on the human brain have yet to be fully understood. In this study, we utilize functional magnetic resonance imaging (fMRI) to evaluate the effect of tPBM on the blood-oxygenation-level-dependant (BOLD) and cerebral blood flow (CBF), while varying specific stimulation parameters such as wavelength, irradiance, and frequency. We further examine the influence of skin tone and sex. Our results show spatially varying fMRI responses to tPBM, with the site of irradiation and more distal sites (including the default-mode network) responding. Certain regions display a sustained fMRI response after tPBM cessation. Furthermore, the responses are dependent on stimulation parameters, sex and skin-tone. Biophysical modeling revealed a temporal dependence of potential neurovascular coupling underlying the tPBM response, one that declined during the course of the stimulation but became elevated immediately after stimulation cessation. This study helps to establish some physiological fundamentals of tPBM and demonstrate the importance of parameter optimization for therapeutic interventions.

bioRxiv preprint doi: https://doi.org/10.1101/2025.11.20.689588; this version posted November 21, 2025. The copyright holder for this preprint (which was not certified by peer review) is the author/funder. All rights reserved. No reuse allowed without permission.

Introduction

Transcranial photobiomodulation (tPBM) is a non-invasive neuromodulation technique that utilizes low-level red or near-infrared (NIR) light to stimulate neural tissue, cellular processes and promote tissue repair (Hamblin 2016). NIR light can penetrate human skin and tissue to various depths ranging several millimeters, giving rise to biological reactions (Zhang et al. 2000), (Wurtman 1975). Specifically, tPBM is known for its ability to increase adenosine triphosphate (ATP) production through the dissociation of an inhibitory nitric oxide (NO) molecule on the cytochrome c oxidase (CCO) enzyme (Thunshelle and Hamblin 2016), (Collman et al. 2008). tPBM is currently in clinical trials for the management of stroke, traumatic brain injury, Parkinson's disease, depression, Alzheimer's disease and other dementias (Montazeri et al. 2021). Recent studies have shown the various positive cognitive effects of tPBM, such as enhancing memory processing, (Chan et al. 2021), improving executive function (Hamblin 2018), as well as enhancing cognitive and emotional brain functioning (Ji et al. 2023). While these effects have been well distinguished in vitro, and through cognitive testing, individual cellular responses can trigger secondary physiological responses, including the modulation of neuronal excitability and cerebral blood flow (CBF) (Jahan et al. 2019). However, despite the growing evidence supporting tPBM as a neuromodulation therapy, the precise physiological mechanisms of tPBM on the human brain remain poorly understood, as tPBM could influence metabolism, oxygen consumption, and perfusion (Hennessy and Hamblin 2017).

Most tPBM publications utilize cognitive testing as the reference for evaluating tPBM outcome. To assess the physiological effects of tPBM on the human brain, several neuroimaging and electrophysiological techniques have been employed, including single-photon emission computed tomography (SPECT) (Baik et al. 2021), functional near-infrared spectroscopy (fNIRS), electroencephalography (EEG), and blood-oxygenation-level-dependent (BOLD) functional magnetic resonance imaging (fMRI). Among these, fNIRS has been the most frequently used in real-time PBM studies, showing time-locked hemodynamic changes at the site of stimulation (Tian et al. 2016). fNRIS is portable and has a quick setup time, but its limited spatial coverage restricts whole-brain interpretation (Holmes et al. 2019). fMRI offers whole-brain coverage and sensitivity to both hemodynamic and metabolic changes (Bandettini 2014), making it particularly well-suited for quantifying tPBM-induced effects on cerebral physiology. Nonetheless, to our knowledge the majority of fMRI studies in PBM have examined the pre-post-PBM differences (Chao 2019) (Naeser et al. 2020), (El Khoury et al. 2019), and little is known about the real-time effects (Dmochowski et al. 2020), (Gaggi et al. 2024). Existing PBM-fMRI studies have shown that tPBM can decrease the fractional amplitude of low-frequency BOLD fluctuations (Gaggi et al. 2024). However, the real-time response of the underlying BOLD signal remains unclear.

BOLD fMRI measures changes in deoxygenated hemoglobin concentrations, which reflect the balance between the cerebral metabolic rate of oxygen ($CMRO_2$) and CBF. Neural stimulation increases $CMRO_2$, accompanied by vasodilation and a corresponding rise in CBF (Lin et al. 2008). However, the interpretation of BOLD with regard to CBF and $CMRO_2$ is ambiguous, and thus combining BOLD and CBF measurements provides complementary insights. tPBM can increase CBF through nitric oxide induced vasodilation, distinguishing the rise in blood flow from oxygen metabolism, and the overarching BOLD response provides the full picture of the hemodynamic response to tPBM. The literature on this topic has been varied. While fNIRS studies of the frontal cortex have widely shown an increase in the concentrations of oxyhemoglobin and total hemoglobin (a surrogate of CBF) due to tPBM (Holmes et al. 2019), a 2021 fMRI study showed that an 810nm irradiation pulsing at 10Hz with an irradiance

bioRxiv preprint doi: https://doi.org/10.1101/2025.11.20.689588; this version posted November 21, 2025. The copyright holder for this preprint (which was not certified by peer review) is the author/funder. All rights reserved. No reuse allowed without permission.

of 250mW/cm² did not induce a significant CBF change in any brain region, (El Khoury et al. 2019). A more recent study showed a significant increase in CBF and $CMRO_2$, but the analysis was limited to the site of illumination (Zhao et al. 2025). In fact, beyond the question of the BOLD and CBF responses in tPBM, there remain many significant gaps in the understanding of how tPBM affects neural activity and vascular responses. For example, is the BOLD response to tPBM focal to the site of illumination more global? How is the BOLD response during tPBM shaped by changes in CBF? Addressing these questions is crucial to broadening the understanding of the effect of PBM on the brain.

Beyond establishing the neurovascular underpinnings of tPBM, it is also important to determine the dose dependence of such a response. Shorter wavelengths have been shown both numerically and empirically to penetrate less deeply than longer near-infrared (NIR) wavelengths (Zein et al. 2018), (Yuan et al. 2020), (Cassano et al. 2019), (Van Lankveld et al. 2025). Moreover, wavelengths around 670 nm and 830 nm are known to correspond to absorption peaks of CCO, the targeted photo-acceptor in the mitochondrial electron transport chain, but wavelengths in the range of 808 to 1064 nm are typically used. Irradiance, the energy of light delivered per unit area (mW/cm²), directly influences energy accumulation in targeted brain regions. Typical irradiance settings for clinical applications range from 250 to 300 mW/cm², staying below the medical safety limit of 330 mW/cm² to avoid tissue damage. Pulsation frequency, specific to pulsed tPBM, is typically set to 10 Hz and 40 Hz to align with the brain's natural alpha and gamma rhythms, respectively, but their effects have yet to be distinguished in vivo. Furthermore, biological factors such as melanin, which also impacts penetration (Setchfield et al. 2024), has never been considered in tPBM.

In this study, we aim to assess data-driven region-specific and real-time BOLD and CBF responses to varied doses of pulsed tPBM in healthy adults. Moreover, based on prior literature and our own simulation studies, we hypothesize that individuals with lighter skin will experience a greater percentage change in BOLD and CBF than those with intermediate or darker skin tones. Additionally, we hypothesize that tPBM will induce a larger percentage change in BOLD and CBF with the 808 nm wavelength compared to 1064 nm. We will also determine the dependence of the tPBM response and the underlying neurovascular coupling on light-pulsation frequency as well as skin tone and sex.

Methods

Participants

We recruited 45 healthy young adults (age 20-32, 23 M/22 F) who were screened prior to their participation to ensure there was no history of neurological or physiological disorders, malignant disease, or the use of medications that could have influenced the study. The Baycrest Research Ethics Board (REB) approved the study, and all experiments were conducted in accordance with REB guidelines, with each participant providing written informed consent.

PBM Instrumentation

The MRI compatible lasers were provided by Vielight Inc. (Toronto, Canada), and the light was delivered through a 10-meter, 400µm optic cable to the MRI, while the laser system remained outside the scanner room. The light parameters, including wavelength, irradiance and pulsation frequency, were controlled from the scanner console while the participant was inside the scanner. To avoid any placebo effects, the participant remained blinded to the stimulation paradigm, the light was secured through a headpiece such that it was not visible to the participants.

bioRxiv preprint doi: https://doi.org/10.1101/2025.11.20.689588; this version posted November 21, 2025. The copyright holder for this preprint (which was not certified by peer review) is the author/funder. All rights reserved. No reuse allowed without permission.

MRI Acquisition

MRI data were acquired using a Siemens Prisma 3 Tesla System (Siemens, Erlangen, Germany) with a 20-channel radio-frequency coil. For each participant, the following data was collected: (a) A T1-weighted structural image (sagittal, 234 slices, 0.7 mm isotropic resolution, TE = 2.9 ms, TR = 2240 ms, TI = 1130 ms, flip angle = 10°). (b) A dual-echo pseudo-continuous arterial spin labeling (DE-pCASL) scan (courtesy of Danny J. J. Wang, University of Southern California) to simultaneously measure cerebral blood flow (CBF) and BOLD (TR = 4.5 s, TE1 = 9.8 ms, TE2 = 30 ms, post-labeling delay = 1.5 s, labeling duration = 1.5 s, flip angle = 90°, 3.5 mm isotropic resolution, 35 slices, 25% slice gap, total scan time = 12 minutes 15 seconds). Additionally, an M0 calibration scan was acquired for CBF quantification, with a TR of 10 s and a scan time of 45 s, while all other parameters remained the same as in the pCASL scan. For n=30 participants, one MR thermometry sequence was acquired (TR = 97 ms, TE1 = 4.92 ms; TE2 = 7.38 ms; FoV = 192 mm; slice count = 10).

Participants were scanned while viewing naturalistic stimuli to minimize variations in brain state across participants, thereby improving the reproducibility of the stimulation outcome (Gal et al., 2022).

Stimulation Protocol

This study varies two wavelengths, three irradiances and two pulsation frequencies, as shown in Table 1. Moreover, we recruited an equal representation of three skin colour groupings (light, intermediate and dark). As a quantitative indicator of skin pigmentation (eumelanin and pheomelanin), the individual typology angle (ITA) of each participant was measured using a CM-600D Spectrophotometer (Konica Minolta). The calculated ITA and pixelated image of the right forehead for each participant is shown in **Figure 1**. Additional details can be found in the Supplementary Materials section **S.1.2**.

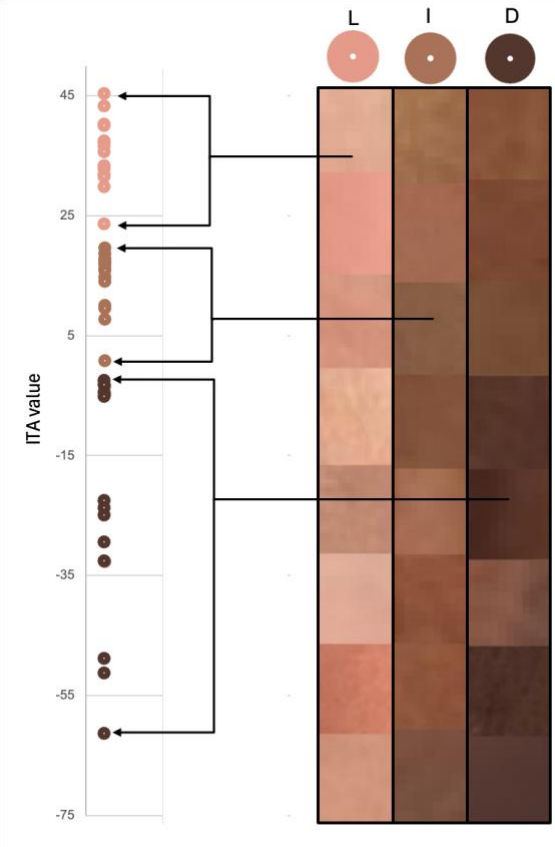

bioRxiv preprint doi: https://doi.org/10.1101/2025.11.20.689588; this version posted November 21, 2025. The copyright holder for this preprint (which was not certified by peer review) is the author/funder. All rights reserved. No reuse allowed without permission.

Figure 1: *Objective measurements of skin tone as compared to photographs of forehead skin for a representative group of subjects. These images were categorized based on their individual typology angle (ITA), to show the general tone of each skin tone grouping L) Light, I) Intermediate and D) Dark. The dots represent the actual ITA values corresponding to the mean visually perceived skin tone based on the individual photos of skin patches which are ordered by ITA in each skin-tone grouping. This is to demonstrate the differences between visually quantifying skin tone compared to a quantifiable metric.*

The tPBM laser was carefully positioned on the right side of the forehead (**Figure 2**), targeting the prefrontal cortex, with two vitamin E capsules placed as fiducial markers of the precise location of irradiation. Each participant was assigned to one of three protocols, with each protocol comprising four scans (see **Table 1**), resulting in 15 participants scanned under each protocol. Each subject underwent 4 tPBM sessions each with a unique combination of dose parameters, as seen in **Table 1**.

Table 1: *Stimulation paradigm for each protocol grouping. The male (M) to female (F) and skin-tone distributions are similar across the three groups. L: light; I: intermediate; D: dark skin.*

Protocol 1			**Protocol 2**			**Protocol 3**		
Wavelength (nm)	**Irradiance (mW/cm²)**	**Frequency (Hz)**	**Wavelength (nm)**	**Irradiance (mW/cm²)**	**Frequency (Hz)**	**Wavelength (nm)**	**Irradiance (mW/cm²)**	**Frequency (Hz)**
1064	100	10	1064	150	10	1064	150	40
808	100	10	808	150	10	808	150	40
1064	200	10	1064	200	40	1064	100	40
808	200	10	808	200	40	808	100	40
Sex	**(M/F)**	8/8			7/7			7/8
ITA	**(L/I/D))**	5/6/5			5/5/4			4/5/6

For each 12-minute scan, the stimulation paradigm was 4-min-OFF, 4-min-ON, 4-min-OFF, as shown in **Figure 2.** A period of at least 10 minutes was provided as a break before each subsequent tPBM session. In combination with the 4 minutes of pre-stimulus recording and 4 minutes of post-stimulus recording there was a minimum time of 18 minutes between stimulations.

bioRxiv preprint doi: https://doi.org/10.1101/2025.11.20.689588; this version posted November 21, 2025. The copyright holder for this preprint (which was not certified by peer review) is the author/funder. All rights reserved. No reuse allowed without permission.

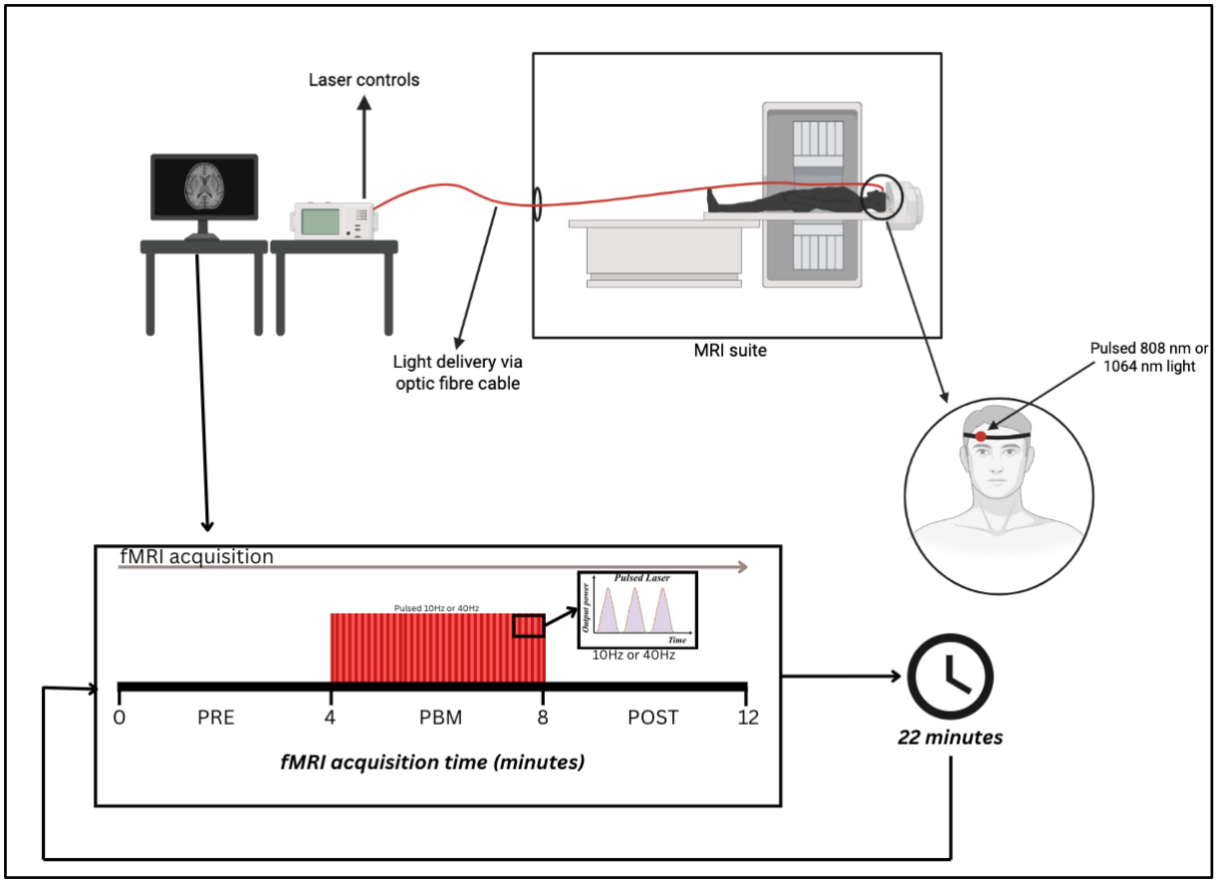

Figure 2: *tPBM-fMRI setup. The optic fibre cable carries the NIR light from the laser control system through a small hole into the MRI suite. The optic fibre is secured to the participants chest strap, fed through the RF coil in the MRI and positioned on the right side of the forehead. From outside the MRI suite, the controls at the console allow the laser to be turned ON/OFF and delivered at the prescribed parameters throughout the fMRI acquisitions. fMRI acquisition follows a 4min-OFF, 4-min-ON, 4-min-OFF paradigm with pulsed NIR light at 10 Hz or 40 Hz.*

MR Thermometry

To test for the existence of brain temperature increases during tPBM, MR thermometry data were collected for the sessions corresponding to the 1064 nm wavelength delivered at the highest irradiance (200 mW/cm²) at both 10 Hz and 40 Hz (N = 30 participants). The full details are provided in Supplementary Materials.

Data Preprocessing

BOLD-fMRI preprocessing was performed using a custom script that employed tools from the FMRIB Software Library (FSL) (Jenkinson et al. 2012), AFNI (Cox 1996), FreeSurfer (Fischl 2012) and MATLAB (The MathWorks Inc., Natick, Massachusetts, USA). The pCASL datasets were brain extracted (FSL bet) and split into their even and odd volumes to separate the control and tag images (FSL slicetimer and FSL fslsplit), motion correction was done separately for the even and odd images. Final BOLD maps were calculated using a surround mean difference approach (Liu and Wong 2005). CBF-fMRI data was preprocessed using ASLprep (Adebimpe et al. 2022). MATLAB was used for temporal and spatial outlier removal, drift correction and normalization. The first five volumes of both BOLD and CBF were rejected to allow the brain to enter a steady state. All datasets were registered and resampled (FSL flirt) into MNI space for group analysis.

bioRxiv preprint doi: https://doi.org/10.1101/2025.11.20.689588; this version posted November 21, 2025. The copyright holder for this preprint (which was not certified by peer review) is the author/funder. All rights reserved. No reuse allowed without permission.

fMRI analysis

Following preprocessing, the data was input into FSL MELODIC (Beckmann and Smith 2004) for an model-free independent component analysis (ICA) regardless of protocol and melanin grouping (N = 180 data sets), as shown in **Figure 3**. The ICA was chosen over the conventional general-linear model (GLM) analysis, as the hemodynamic response function for tPBM remains unknown.

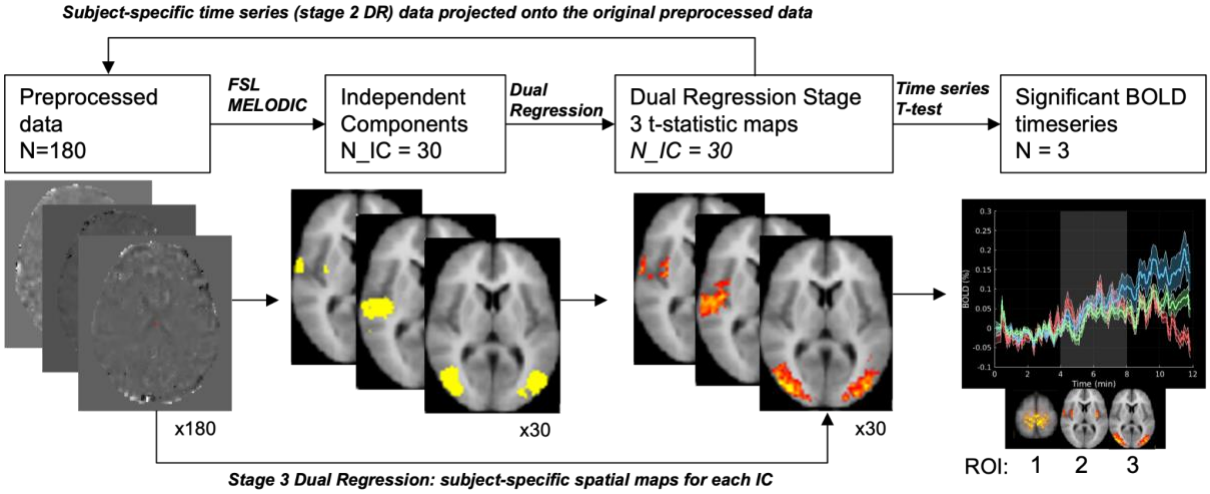

Figure 3: *Independent component analysis and subsequent dual regression for generating the regions of interest (ROIs). All resulting independent components (ICs) were then t-tested for significance and the five remaining ICs were selected as the final ROIs.*

The number of independent components (ICs) was set to 30 to avoid fragmentation. The ICs were normalized and their temporal characteristics were examined through a t-test to determine significant correspondence with the onset of the tPBM stimulus. Subsequently, dual regression was performed to map the ICs to the normalized individual subject time series and experimental conditions. The dual regression model consists of three stages, generating statistical maps and time series for each IC, allowing for subject-specific characterization of BOLD dynamics and spatial specificity. Each of these ICs was taken as a region of interest (ROI). After dual regression, the subject-specific BOLD-normalized and CBF-normalized time series for each ROI and the site of illumination, were plotted to visualize the dynamic temporal changes in BOLD and CBF signals across conditions. To determine whether the observed BOLD and CBF signal changes were statistically significant during stimulation, we conducted a t-test on the rise of the time course within the defined experimental paradigm (4 minutes OFF, 4 minutes ON, 4 minutes OFF).

Mixed-Effects Modeling

The %BOLD and %CBF change relative to the pre-stimulus period was calculated and input into a t-test for the periods during and post stimulation. These average t scores were incorporated into a linear mixed-effects (LME) model as the dependent variable to analyze the influence of irradiance, wavelength, frequency, melanin level (ITA) and sex on BOLD and CBF responses. However, if the time series did not exhibit a statistically significant change, the %BOLD and %CBF change for that condition was set to zero, ensuring that non-significant responses did not contribute to the statistical modeling.

The LME model followed a two-step approach. First, we used MATLAB's stepwise LME (stepwiselm) function to identify parameter variables that had no significant effect ($p >$

bioRxiv preprint doi: https://doi.org/10.1101/2025.11.20.689588; this version posted November 21, 2025. The copyright holder for this preprint (which was not certified by peer review) is the author/funder. All rights reserved. No reuse allowed without permission.

0.05, False Discovery Rate (FDR)-corrected) on the temporal BOLD and CBF response. These variables were removed from the final LME to maximize information content of the remaining fixed effects. The final model followed the following format, where the subject was included as a random variable.

$$\%BOLD \sim Variable_a + Variable_b + Variable_a * Variable_b + (1\,|Subject)$$

Wavelength, irradiance, pulsation frequency and sex were set as categorical variables, and ITA as a continuous variable. Final statistical p-values were thresholded with FDR correction.

BOLD Biophysical Modeling

To further characterize the relationship between BOLD and CBF, we fit the temporal mean BOLD and CBF responses from each scan of each subject to the deoxyhemoglobin dilution model as shown in Eq. 1 (Davis et al. 1998), with set parameters β=1.3, α=0.2 (Hare et al. 2015). The relationship between CBF and $CMRO_2$ was defined by Eq. 2 (Hoge et al. 1999),

$$\frac{\Delta BOLD}{BOLD_0} = M\left(1 - \left(\frac{CMRO_2}{CMRO_{2,0}}\right)^{\beta}\left(\frac{CBF}{CBF_0}\right)^{\alpha-\beta}\right) \quad (1)$$

$$\Delta CBF = n * \Delta CMRO_2 \quad (2)$$

where changes in CBF and $CMRO_2$ are related by the neurovascular coupling ratio n. Both the n-value and M-value were derived from the above model, where the M-value estimated from the first time window was then used in the two subsequent windows to fit for the n-values. This was performed for each ROI separately. To reduce noise and stabilize the CBF-BOLD relationship prior to model fitting, the data was stratified into bins of 6 points. For each condition, all observations were sorted into ascending order based on their stimulus-BOLD response mean. Within each bin, the mean BOLD and CBF signal were computed, yielding a single representative value per 6 data points.

Results

MR thermometry

Group-level statistical comparison against the pre-stimulus (minutes 1-4) and the stimulus (minutes 5-8) was conducted across both stimulation frequencies to show that the average temperature change was minimal and remained stable over the entire 12 minutes, as shown in **Table 2**. This confirms that even at the longest wavelength and highest irradiance used, no measurable thermal effects were produced in the illuminated brain region. Please see **Figure** S2 in Supplementary Materials for details on the definition of the illuminated region.

Table 2: Group-level statistical comparison of MR-thermometry-based temperature changes between PBM and the PRE-stimulus recording and standard deviation (STD) for both stimulation frequencies (10 Hz and 40 Hz).

Frequency	PRE (°C)	PRE STD (°C)	PBM (°C)	PBM STD (°C)	p-value
10 Hz	-0.0161	0.1820	0.0501	0.1645	0.13

bioRxiv preprint doi: https://doi.org/10.1101/2025.11.20.689588; this version posted November 21, 2025. The copyright holder for this preprint (which was not certified by peer review) is the author/funder. All rights reserved. No reuse allowed without permission.

40 Hz	-0.0016	0.1581	0.0087	0.1540	0.76

BOLD fMRI responses

The model-free analysis across all data sets revealed 3 ROIs that were associated with the tPBM timing vector based on visual inspection. Additional information regarding the ICA and dual regression approach can be found in the first section of the supplemental materials.

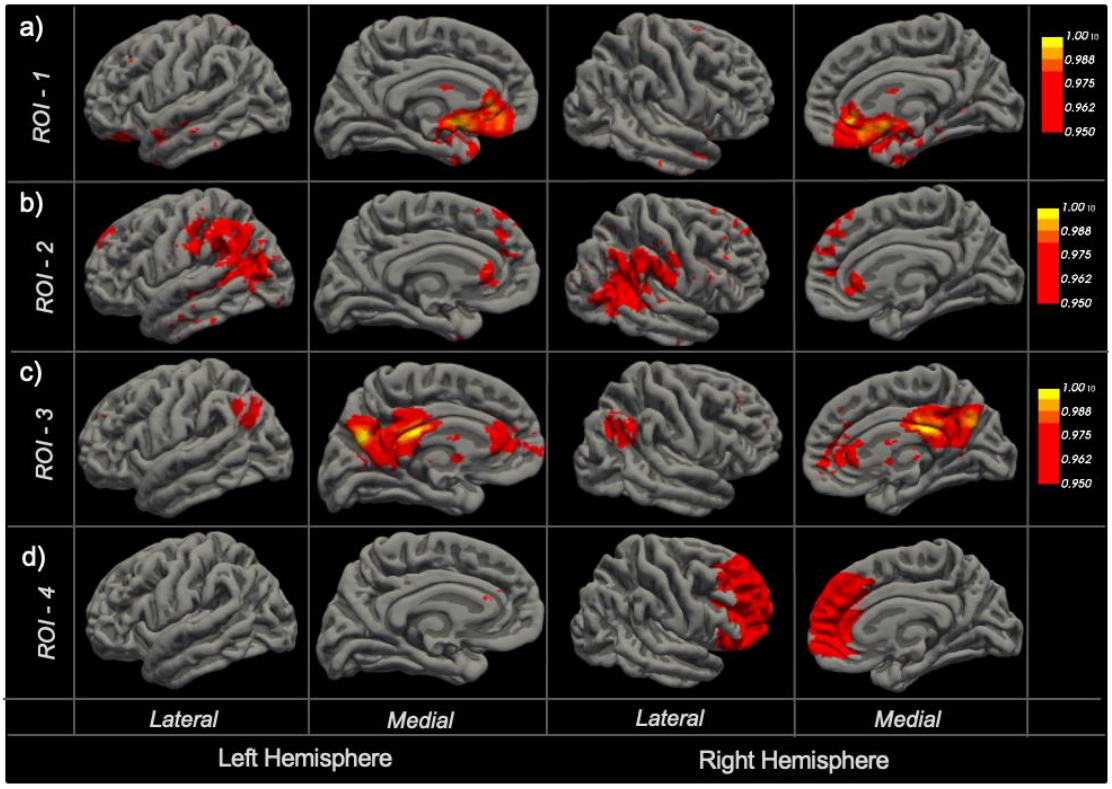

Figure 4: *a-c) ROIs 1-3, which are Independent components showing a significant BOLD fMRI response, derived from ICA followed by dual regression, thresholded to $p < 0.05$. Highlighting specific brain areas most consistently associated with the PBM effects, irrespective of subject or stimulation parameter. d) ROI 4, which is the site of stimulation (illumination), manually selected per participant (see Supplemental Materials* ***S.1.3****) and averaged across all. All ROIs are mapped from native to MNI space, and shown on the medial and lateral surfaces. Only voxels with t-values corresponding to $p < 0.05$ are displayed, the colour bar represents voxels with stronger and more consistent positive spatial associations within the ROI across individual subjects.*

Three ICs survived the ICA step and are shown in **Figure 4**, with the anatomical and functional determinants of ROIs 1-3 obtained from NeuroSynth (correlation coefficients (r) listed below) (Yarkoni et al. 2011):

- ROI 1 (**Figure 4a**) consists of subgenual (r = 0.55), accumbens (r = 0.45), and ventromedial prefrontal (r = 0.43), which are associated with mood regulation and emotional processing;
- ROI 2 (**Figure 4b**) consists of the posterior superior (r = 0.31), the temporal (r = 0.30), and the temporal sulcus (r = 0.298), which are involved in information processing;
- ROI 3 (**Figure 4c**) consists of the posterior cingulate (r = 0.56), the precuneus (r = 0.46), and the default mode network (r = 0.35) which are associated with cognitive functioning, emotional regulation, and memory.

bioRxiv preprint doi: https://doi.org/10.1101/2025.11.20.689588; this version posted November 21, 2025. The copyright holder for this preprint (which was not certified by peer review) is the author/funder. All rights reserved. No reuse allowed without permission.

- ROI 4 (**Figure 4d**) represents the illuminated region, which was defined as the region most proximal to the light's incidental site, as described earlier and in **Figure S1**. The subject-specific regions were averaged across all subjects to provide the most generalizable mask for the site of stimulation.

To characterize the temporal regional responses of each ROI, we extracted the BOLD signal trajectory in each ROI by computing the average BOLD intensity across all active voxels. The time series for each region is shown in **Figure 5**.

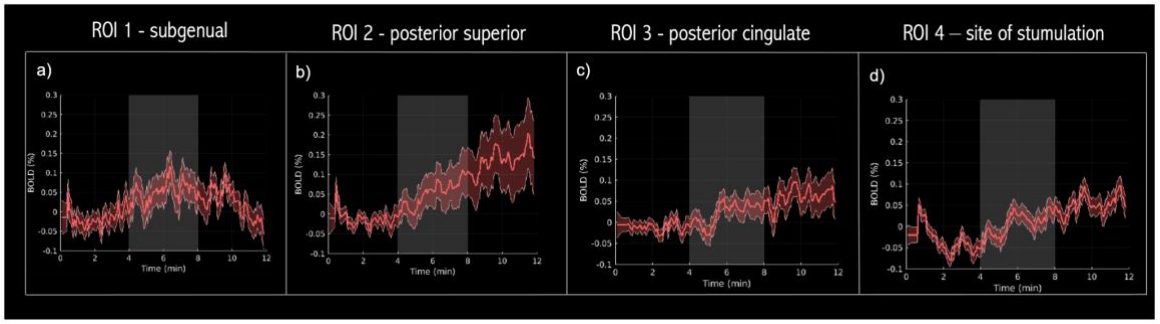

Figure 5: *Mean BOLD time series from each ROI defined in Figure 4. Coloured shaded regions represent the standard error across all datasets. The tPBM stimulus "on" period (minutes 4:8) is denoted by the shaded grey region.*

bioRxiv preprint doi: https://doi.org/10.1101/2025.11.20.689588; this version posted November 21, 2025. The copyright holder for this preprint (which was not certified by peer review) is the author/funder. All rights reserved. No reuse allowed without permission.

Linear Mixed Effects Modelling

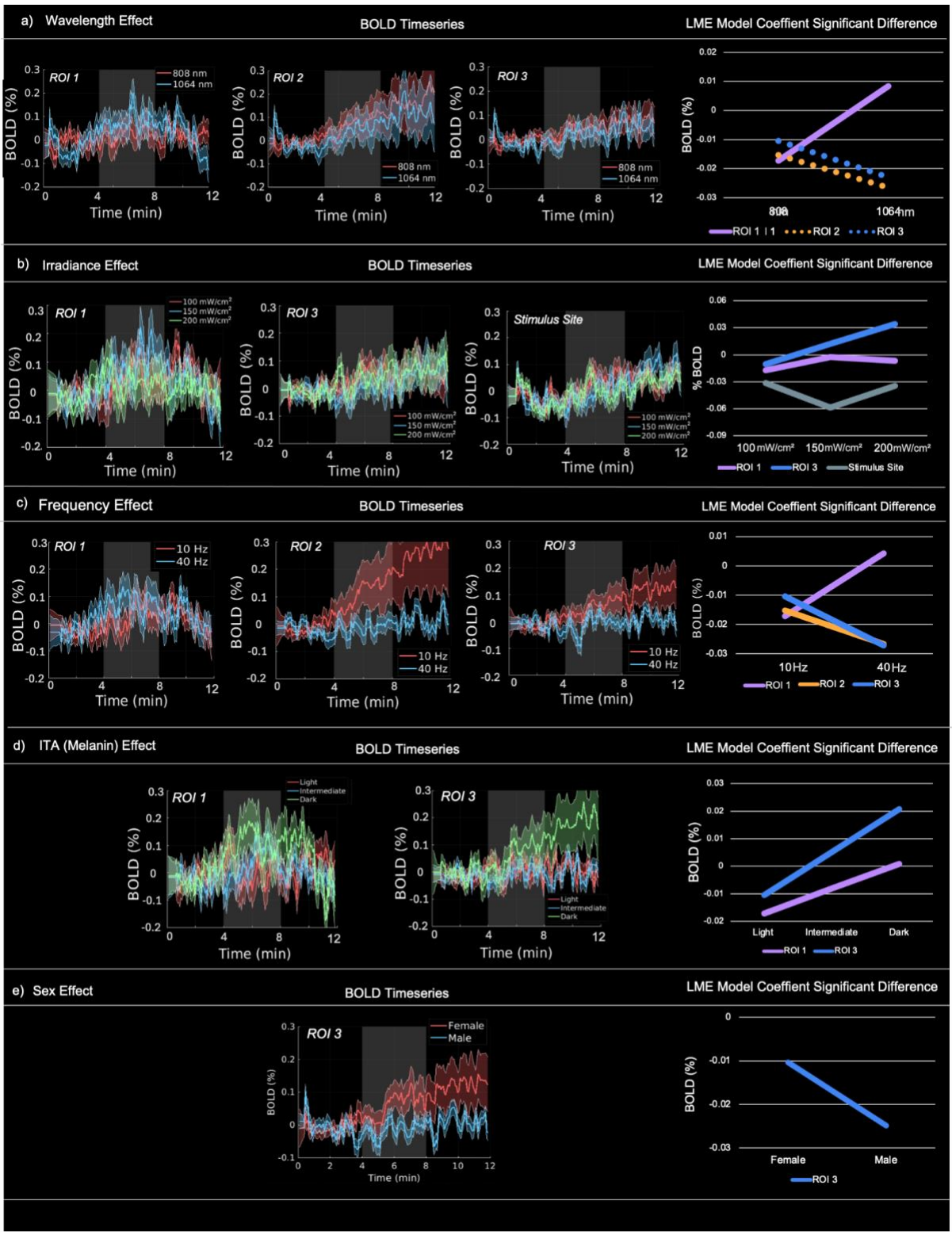

Figure 6. *BOLD temporal response magnitudes across stimulation parameters. The y-axis represents response magnitude from the average for each ROI, reflecting the LME model response derived from 180 inputs and grouped by wavelength, irradiance, sex, frequency, and ITA level. All lines represent statistically significant changes ($p < 0.05$), solid lines reflect LME statistical differences between the PRE-stimulus window (minutes 0:4) and stimulus window (minutes 4-8), dashed lines reflect LME statistical differences between the PRE-stimulus*

bioRxiv preprint doi: https://doi.org/10.1101/2025.11.20.689588; this version posted November 21, 2025. The copyright holder for this preprint (which was not certified by peer review) is the author/funder. All rights reserved. No reuse allowed without permission.

window (minutes 0:4) and the POST-stimulus window (minutes 8:12), with the shaded regions reflecting the standard error of each timeseries. Each colour represents a distinct region of interest (ROI 1, 2 or 3).

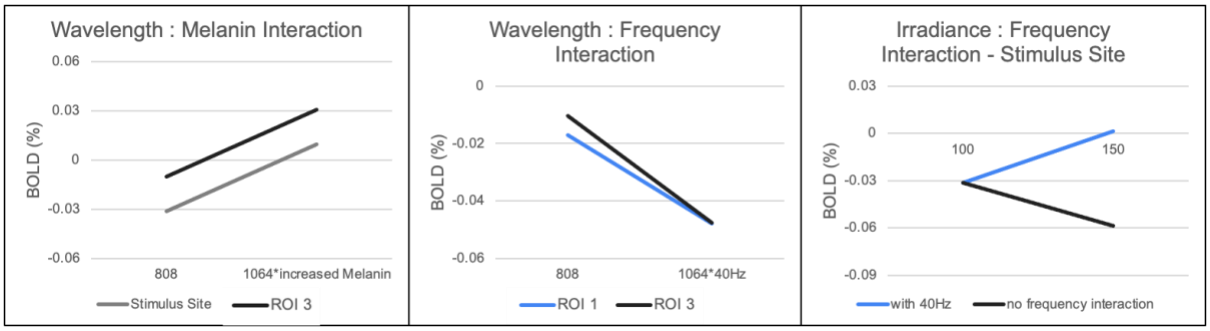

Figure 7. *BOLD temporal response magnitudes across the interaction of stimulation parameters. The y-axis represents response magnitude from the average for each ROI, reflecting the LME model response derived from 180 inputs and grouped by wavelength, irradiance, frequency, and ITA level. All lines represent statistically significant changes ($p < 0.05$).*

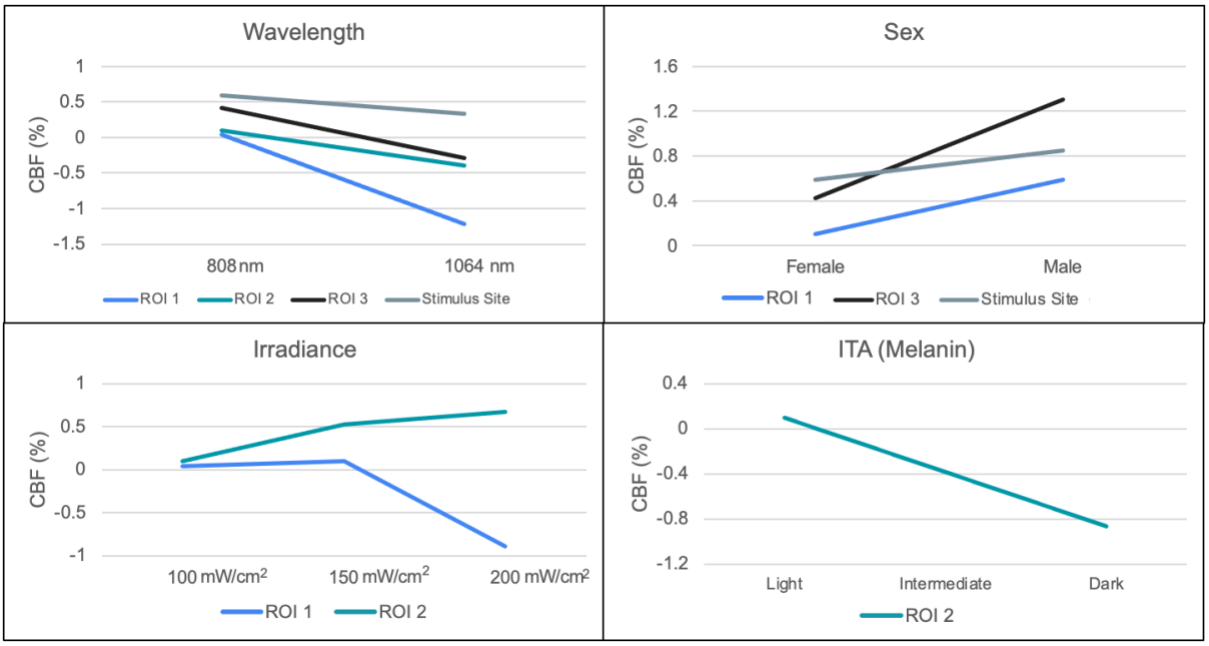

Figure 8. *The dose and biological dependence of the CBF response. The y-axis represents response magnitude from the average for each ROI, reflecting the LME model response derived from 180 inputs and grouped by wavelength, irradiance, frequency, and ITA level. All lines represent statistically significant changes ($p < 0.05$). Each color represents a distinct region of interest (ROI 1, 2 or 3).*

The LME modelling highlighted the ROIs exhibiting a significant temporal response magnitude between various stimulation parameters, a summary of all responses are shown in **Table 3** below. In addition to the statistical effects, we report the mean % BOLD increase during stimulation for ROI 1, and the post stimulation mean %BOLD for ROIs 2-4. We also include a normalized metric of efficiency, where the %BOLD signal is standardized by irradiance. For each individual session (n = 180), the mean % BOLD response is calculated and then divided by corresponding irradiance (100, 150, 200 mW/cm²), allowing comparison of response strength relative to the delivered optical power density.

bioRxiv preprint doi: https://doi.org/10.1101/2025.11.20.689588; this version posted November 21, 2025. The copyright holder for this preprint (which was not certified by peer review) is the author/funder. All rights reserved. No reuse allowed without permission.

Table 3: *ROI-level statistical summary results from the Linear Mixed Effects model of stimulation parameters for both a) BOLD and b) CBF. ITA breakdown: L/I/D = Light, Intermediate, Dark)*

a)

					% BOLD				
ROI	Location	Time series	% BOLD increase	Efficiency (% BOLD /mW/cm^2)	Wavelength (nm)	Frequency (Hz)	ITA	Irradiance (mW/cm^2)	Sex
1	subgenual / accumbens	Block response	0.117% SE = 0.043	2.8×10^{-4} % SE = 1.3×10^{-4}	1064 > 808	40 > 10	L < I < D	100 < 150 > 200	-
2	posterior superior / temporal sulcus	Ramp	0.205 % SE = 0.093	1.57×10^{-4} % SE = 1.8×10^{-4}	1064 < 808	40 < 10	-	100 < 150 < 200	Female > Male
3	posterior cingulate / DMN	Ramp	0.09 % SE = 0.043	2.95×10^{-4} % SE = 1.8×10^{-4}	1064 < 808	40 < 10	L < I < D	100 > 150 < 200	-
4	stimulus site / prefrontal cortex	Ramp	0.147% SE = 0.0268	2.17×10^{-4} % SE = 8.0×10^{-5}	-	-	-	-	-

b)

		% CBF			
ROI	Location	Wavelength (nm)	ITA	Irradiance (mW/cm^2)	Sex
1	subgenual / accumbens	1064 < 808	-	100 < 150 > 200	-
2	posterior superior/temporal sulcus	1064 < 808	L > I > D	100 < 150 < 200	Male > Female
3	posterior cingulate / DMN	1064 < 808	-	-	Male > Female
4	stimulus site / prefrontal cortex	1064 < 808	-	-	Male > Female

Biophysical Modeling

To further quantify the neurovascular mechanism underlying the observed BOLD and CBF responses using the biophysical BOLD model, we determined the slope between CBF and BOLD mean responses across participants in all four ROIs, and for different time windows in the stimulation and post-stimulation period. These time-window averages are shown for all scans of all subjects in the scatter plots shown in **Figure 9a**. In general, regions showing increased BOLD responses also demonstrated proportional increases in CBF. This is summarized in **Figure 9b.** Moreover, it can be seen that the BOLD-CBF slope decreases with advancing time both during PBM stimulus and post-PBM stimulus.

bioRxiv preprint doi: https://doi.org/10.1101/2025.11.20.689588; this version posted November 21, 2025. The copyright holder for this preprint (which was not certified by peer review) is the author/funder. All rights reserved. No reuse allowed without permission.

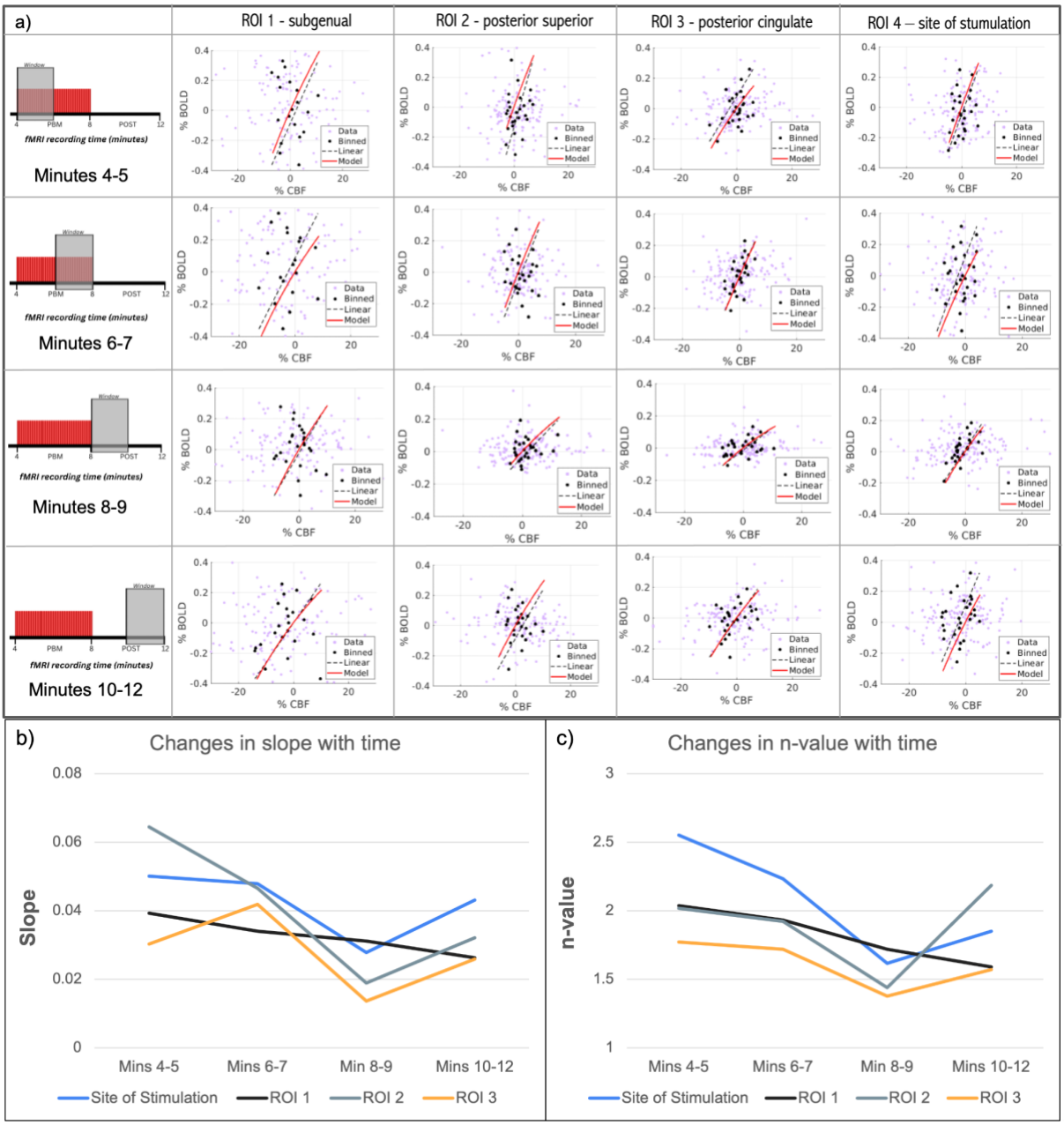

Figure 9: *The relationship between BOLD and CBF responses across ROIs was evaluated using a neurovascular coupling model derived from the average BOLD and CBF response. (a) Scatter plot of the temporal mean BOLD and CBF responses from each scan of each subject, derived from the deoxyhemoglobin dilution model (Eq.1). The data were stratified into bins of 6 data points, and each dot represents the mean of one bin. ((b) BOLD-CBF slope for each ROI, in time windows. c) n-value variations with time window for all ROIs.*

The n-values were estimated by modeling the measured BOLD using the CBF responses, and reflects the relationship between CBF and $CMRO_2$. The average n-value was calculated to be 2.04 +/- 0.59 (ROI 4, i.e. site of illumination), 1.78 +/- 0.41 (ROI 1), 2.12 +/- 0.76 (ROI 2) and 1.61 +/- 0.23 (ROI 3). The variations in the estimated n value **(Figure 9b)** follow those of the BOLD-CBF slopes.

Discussion

Currently, a major barrier in achieving broader clinical translation of tPBM is the limited understanding of its physiological mechanisms and the associated dose dependence. In this work, we utilized BOLD- and CBF-fMRI to characterize the real-time regional cerebral

bioRxiv preprint doi: https://doi.org/10.1101/2025.11.20.689588; this version posted November 21, 2025. The copyright holder for this preprint (which was not certified by peer review) is the author/funder. All rights reserved. No reuse allowed without permission.

hemodynamics to tPBM across various stimulation parameters, different sexes and skin tones. Our main findings are: (1) the fMRI response to tPBM is not constrained to the site of stimulation, but is instead distributed across brain regions; (2) the tPBM-evoked fMRI response did not follow a uniform temporal profile; in some regions it closely tracked the stimulation period, whereas in others in remained elevated after stimulation; (3) parameter associations were regionally dependent; with varied responses for BOLD and CBF, conditions maximizing the BOLD response (sex and ITA) minimized the CBF response; (4) the response also depended on skin tone and sex; (5) the BOLD fMRI response to tPBM generally suggests a contribution by CBF, but the BOLD-CBF relationship varied with stimulation time period. These results were found to be independent from any thermal mechanism as demonstrated in our MR thermometry section in Results and Supplementary Materials.

Spatial distribution of BOLD response to tPBM

Our results show a BOLD response at the site of stimulation, consistent with the current literature, however, the response at the site of stimulation was the smallest BOLD response shown. Greater BOLD responses are found in ROIs beyond the site of stimulation, in our case the subgenual and accumbens (ROI 1), the posterior superior temporal sulcus (ROI 2) as well as the default mode network including the posterior cingulate (ROI 3). The largest BOLD response was detected in ROI 2, followed by the subgenual and posterior cingulate. Past findings showed that tPBM altered FC in these regions (Dmochowski et al. 2020), and we speculated that the increases in the BOLD fMRI signal are mediated through similar mechanisms as the increase in FC, with an enhanced CBF and modulated cerebral oxygenation. Specifically, functional networks may play a role.

The posterior superior/temporal sulcus regions are highly connected with the prefrontal cortex (site of stimulation) (Garell et al. 2013), forming part of a broader functional network (default-mode network). These connections may facilitate the sequential activation of distal nodes following prefrontal stimulation, a phenomenon previously also reported in transcranial magnetic stimulation (Vink et al. 2018). Furthermore, In our recent work, we dissect the sequence of this propagation (Chen et al. 2025). We noted that BOLD increases appeared in the medial and lateral prefrontal cortices immediately upon tPBM onset, with subsequent activation emerging in regions associated with the default-mode network; the precuneus, posterior cingulate cortex, and hippocampus responding over the next 40-100 s. we also observed such lagged response patterns in other networks. These delayed and spatially structured responses suggest that tPBM engages distributed functional networks that evolve over time, rather than acting locally at the site of stimulation.

Temporal dynamics of BOLD response to tPBM

In our analysis, we did not assume the canonical hemodynamic response, but rather used a model-free approach. This analysis yielded two distinct temporal patterns, depending on the ROI, as shown in **Figure 5**. ROI 1 demonstrates a block pattern corresponding largely to the onset and offset times of our light stimulus. This shape has been noted in previous BOLD-fMRI (Zhao et al. 2025) and functional connectivity studies (Dmochowski et al. 2020), but is inconsistent with the vast body of fNIRS literature, which report a sustained post-stimulus hemodynamic response (Saucedo et al. 2021), (Truong et al. 2022). Interestingly, the BOLD responses in ROIs 2-4 (including the site of illumination) all exhibit a more sustained BOLD response shape. This prolonged response has also been seen in the literature through oxyhemoglobin (HbO) concentration with fNRIS (Urquhart et al. 2020). Moreover, a change in deoxyhemoglobin concentration at 3 Tesla corresponds approximately 0.055% of the

bioRxiv preprint doi: https://doi.org/10.1101/2025.11.20.689588; this version posted November 21, 2025. The copyright holder for this preprint (which was not certified by peer review) is the author/funder. All rights reserved. No reuse allowed without permission.

baseline BOLD signal change, consistent with the magnitude of %BOLD responses observed in our study (Huppert et al. 2008).

The fNRIS literature suggested that the combination of increased mitochondrial activity and NO-mediated vasodilation leads to elevated blood flow and oxygen delivery, producing a sustained increase in Δ[HbO] that continues post-stimulus. This was indeed the case for our BOLD responses at the site of stimulation. However, unlike in fNIRS, fMRI allows measurements from sites well beyond the site of stimulation, which allows us to see a different response.

More distal brain regions follow a different response shape. Notably, the time-locked response in the subgenual-accumbens-ventromedial prefrontal cortex (ROI 1) was never reported in fNIRS studies. A similar response shape was previously reported by Zhao et al. (Zhao et al. 2025), albeit using continuous PBM and in the frontal lobe. This response is more rapid to recover to baseline, and suggests the participation of a transient activation of ion channels that regulate neuronal excitability. These channels are often triggered by longer wavelengths (+ 980 nm), (Y. Wang et al. 2017), (Zupin et al. 2024) (Yan et al. 2025)reflective of our response in ROI 1 showing significant BOLD activation at 1064 nm compared to 808 nm, as well as the 1064.17 nm laser used by Zhao et al. tPBM can trigger responses of calcium, potassium and sodium ions as well as transient receptor potential (TRP) channels. These effects can modulate cellular excitability and influence neuronal and vascular function, by increasing metabolic activity and releasing vasoactive messengers which by extension increase blood flow, (Zhang et al. 2024). These channels operate on a millisecond timescale, opening and closing rapidly in response to depolarization events, but their collective activation during PBM produces sustained neuronal and vascular effects, measurable by fMRI. Light-induced activation of ligand-type sodium channels and TRP channels enhances neuronal excitability and calcium entry, further amplifying metabolic demand. Further investigations are needed to clarify the sources of these different BOLD temporal dynamics.

BOLD response dose dependence

In PBM research, there is currently no response-driven dose optimization. More recently, there have been efforts to model the light penetration into the human brain (Yuan et al. 2020), (Cassano et al. 2019), (Van Lankveld et al. 2025). These simulation results suggest that the 808nm wavelength provides deeper penetration than to the 1064nm and 670nm wavelengths, resulting in greater energy accumulation. The simulations also predict a linear dependence of energy deposition on irradiance. However, cell-culture studies have shown a bi-phasic dependence on irradiance, with both lower and higher levels showing a smaller response in mitochondrial activity and cellular metabolism than that of an intermediate irradiance (Huang et al. 2011). Nonetheless, cellular models cannot account for the light scattering and absorption of different tissues prior to reaching the cranium. This work shows a clear dose dependence for the tPBM BOLD response, but this dose dependence was also region-dependent. When targeting the temporal sulcus and posterior cingulate, 808 nm produced the largest BOLD amplitude, while in the subgenual ROI, 1064 nm produced the highest BOLD temporal responses (**Figure 6a, Table 3a**). Irrespective of the mechanism, it is likely that 808 nm is not always the optimal irradiation wavelength.

Moreover, our results suggest a biphasic irradiance dependence in anterior regions close to the site of stimulation. In ROI 1, the response peaks at 150 mW/cm² and in ROI 4 the response is opposite with the peak at 100 mW/cm² and 200 mW/cm². However, in ROI 3, further from the source of stimulation, a linear response to irradiance is noted, with the 200 mW/cm² producing the largest BOLD response (**Figure 6b**). ROI 3 is mainly associated with

bioRxiv preprint doi: https://doi.org/10.1101/2025.11.20.689588; this version posted November 21, 2025. The copyright holder for this preprint (which was not certified by peer review) is the author/funder. All rights reserved. No reuse allowed without permission.

the default-mode network, which lies deeper in the brain compared to the anterior regions of ROI 1 and 4.

Beyond spatial proximity to the light source, the spatial variations in dose dependence are also dependent on pulsation frequency. That is, in ROIs 2 and 3, the ramp response is generally preferential to one of the frequencies, and this may be in part motivated by the intrinsic oscillatory properties and dominant electrophysiological bands of each region. For instance, the subgenual cortex (ROI 1), which demonstrates the block pattern temporal dynamics at 40 Hz tPBM, is primarily associated with theta (4-8 Hz) and alpha (8-12) Hz rhythms (McCormick et al. 2009). Therefore, higher pulsation frequency (40 Hz) may more effectively drive or disrupt neuronal connections in this ROI, producing transient BOLD changes rather than sustained BOLD increases (**Figure 6c**). In contrast, the posterior-superior temporal sulcus (ROI 2), which is alpha-dominated with task-evoked gamma rhythms, (Nourski et al. 2021) showed a sustained ramp response in the BOLD signal that was sustained post-stimulation, but more pronounced at 10 Hz. Likewise, the posterior cingulate cortex (ROI 3), which is equally dominated at baseline by lower frequencies (delta activity) (Liu et al. 2017), exhibited a smaller but prolonged ramp response at 10 Hz tPBM, consistent with its role in large-scale network coordination (Foster and Koslov 2025). Of course, beyond its dominant baseline rhythm, each region's BOLD response amplitude and shape are also likely driven by its neurovascular responsiveness.

Biological factors

The relationship between skin pigmentation and hemodynamic response was examined using the ITA as an indicator of melanin content. Notably, significant effects of ITA were observed across multiple ROIs, suggesting that skin tone modulates the response to PBM, as predicted by our simulations (Van Lankveld et al. 2025). In ROI 1 (subgenual), and ROI 3 (posterior cingulate), individuals with darker skin tones (lower ITAs) exhibited greater BOLD responses compared to those with lighter or intermediate pigmentation (**Figure 6d**). If we assume that a greater BOLD response is more desirable, then this finding suggests that lighter skin tones, leading to greater energy deposition in brain tissue, is not necessarily optimal. Conversely, in ROI 2 (posterior superior temporal sulcus), individuals with darker skin exhibited lower CBF responses, suggesting the opposite, albeit that ROI 2 was not directly irradiated. In our previous work, we explored the manner in which the BOLD response propagates from the site or irradiation to more distal brain regions (Chen et al. 2025). It is likely proximal and distal regions may undergo somewhat different physiological responses, as will be further discussed below. Moreover, these findings differ from predictions based on Monte Carlo simulations (Van Lankveld et al. 2025), highlighting the importance of in vivo experiments in determining tPBM dose dependence. These findings also underscore the importance of accounting for individual melanin differences when designing PBM protocols and future devices, particularly when targeting consistent effects across diverse populations.

A significant sex effect was also observed in the responses, but only in ROI 3, with a higher BOLD response noted in females compared to the males (**Figure 6e**). This difference could be driven by anatomical factors such as skull thickness, which may modulate light transmission during PBM. Women typically exhibit greater frontal bone thickness than men (Ekşi et al. 2020), which could influence cortical light penetration and contribute to observed sex-specific differences. This finding may also reflect sex differences in baseline CBF and potentially in neurovascular coupling. Females generally exhibit higher resting CBF (Gur and Gur 1990) and stronger neurovascular regulation. Across regions 1-3, males demonstrated a higher CBF response compared to females (**Figure 8**), suggesting that despite a lower resting CBF, males may experience a proportionally greater vasodilation. These patterns could indicate

bioRxiv preprint doi: https://doi.org/10.1101/2025.11.20.689588; this version posted November 21, 2025. The copyright holder for this preprint (which was not certified by peer review) is the author/funder. All rights reserved. No reuse allowed without permission.

sex-dependant differences in cerebrovascular reserve or metabolic demand (Miller et al. 2019). Again, these findings highlight limitations in simulation-driven dose optimization and the complexities of the in vivo PBM response.

The role of CBF

Despite the common assumption that a greater BOLD response is more desirable, the interpretation of the BOLD response is impossible without an understanding of the underlying physiological signals (e.g. CBF and $CMRO_2$) This study is the first to show evidence of a PBM-driven CBF response across multiple brain regions in real time using MRI. In all regions, we see an increase in %BOLD immediately after the onset of stimulation, reflecting an initial hemodynamic response to neural activity, whether this response is sustained past the stimulation period or returns to baseline. This is reflected in a steep BOLD-CBF slope during the first two minutes of stimulation (**Figure 9a**), suggesting a substantial increase in local blood oxygenation that may arise from a CBF increase. This early phase likely reflects robust arterial dilation and is consistent with the past observations of increased Δ[HbO] using fNIRS (Tian et al. 2016).

The two distinct temporal patterns of BOLD responses suggest two scenarios of neurovascular interactions, as detailed below (**Figure 10**).

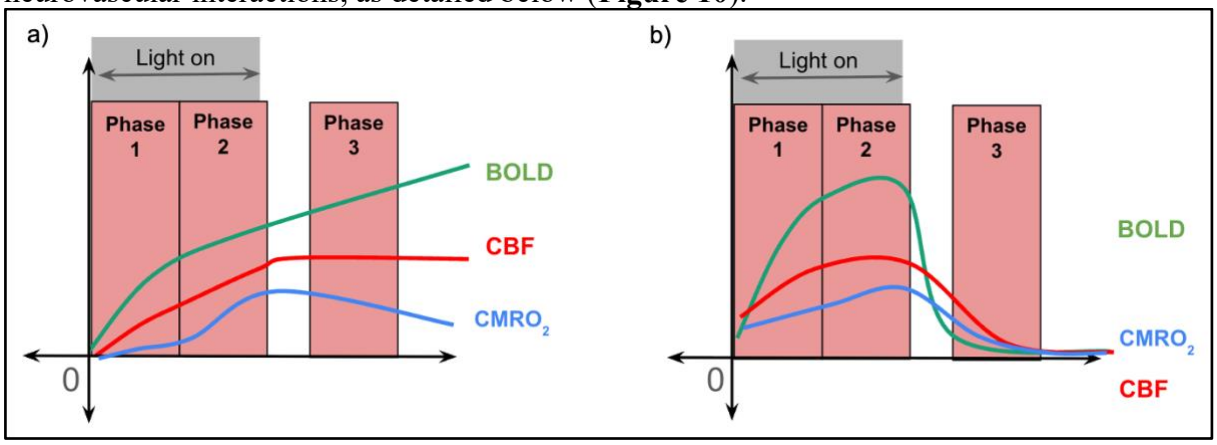

Figure 10: *Hemodynamic and metabolic responses to tPBM across (a) scenarios 1 and (b) scenario 2. Temporal evolution of the BOLD signal (green), CBF signal (red) and $CMRO_2$ (blue) shown across the PBM stimulus (grey region - phase 1 and 2) and post stimulus recording (phase 3).*

Scenario 1: ROIs 2, 3 and site of stimulation (ROI 4)

In ROIs 2, 3 and the site of stimulation, the BOLD response persistently climbed, not returning to baseline even after stimulus cessation (Fig. 10a). This rise in the BOLD signal would have to be supported by a rise in CBF that is proportionally greater than that of $CMRO_2$, producing a net rise in oxygenated hemoglobin ΔHbO concentration, and a relative reduction in deoxyhemoglobin (ΔHb) (Phase 1). During the course of the PBM stimulus, there is a gradual decrease in n-value and BOLD-CBF slope, suggesting a reduction in the CBF increase relative to the $CMRO_2$ increase (Phase 2). After the stimulation ends, $CMRO_2$ begins to decline as metabolic demand gradually returns to baseline (Phase 3). This is consistent with previous reports of similar behaviour in oxidated CCO concentration (X. Wang et al. 2017). However, CBF remains elevated due to delayed vascular recovery and sustained vasodilation. This is also consistent with previous reports of ΔHbO behaviour based on fNIRS (Tian et al. 2016). This is also reflected in the rebound in the n-value post stimulation (**Figure 9b, 9c)**.

The apparent change in coupling between CBF and $CMRO_2$ (a declining n value during stimulation followed by a rise in n-value post-stimulation) suggests that CBF and $CMRO_2$

bioRxiv preprint doi: https://doi.org/10.1101/2025.11.20.689588; this version posted November 21, 2025. The copyright holder for this preprint (which was not certified by peer review) is the author/funder. All rights reserved. No reuse allowed without permission.

responses may not be fully coupled. Regionally, these dynamics likely reflect each region's baseline metabolic and electrophysiological profile, as discussed in the dose-dependence section regarding dominant oscillatory bands and pulsation frequencies. The regional hemodynamic response to tPBM can depend on regional baseline ATP, oxygen and glucose metabolism state as well as oscillatory profile. Regions that consume more oxygen at baseline, or exhibit more high-frequency neural activity (such as gamma rhythm), may show stronger or more sustained hemodynamic effects to tPBM. As tPBM boosts mitochondrial activity and CBF, if a region is already metabolically active, the hemodynamic effect is amplified. In this regard, both the posterior superior temporal sulcus (ROI 2) and the prefrontal cortex (ROI 4), have a high resting metabolic rate (Yang et al. 2023), and are dominated by beta and gamma oscillations (Lundqvist et al. 2016). The posterior cingulate (ROI 3) is part of the default-mode network, demonstrating high resting glucose and oxygen consumption (Passow et al. 2015; Raichle et al. 2001). tPBM in these regions may therefore produce this sustained hemodynamic response, as tPBM further enhances metabolism, when the stimulation ends, the metabolic demand returns to baseline, but CBF remains elevated. This sustained CBF may reflect the sustained involvement of an alternative vascular pathway independent of $CMRO_2$, or serve to remove metabolic waste generated during the period of heightened oxidative metabolism.

Scenario 2: ROI 1

The BOLD response in ROI 1 follows a more conventional trajectory that resembles the block design. There is no maintained post-stimulus BOLD response, and no rebound in the n-value (Phase 3). This suggests that the increased CCO oxidation fuels neuronal activity, leading to the appearance of a tighter neurovascular coupling. Nonetheless, like in Scenario 1, both the BOLD-CBF slope and modeled *n*-value steadily decreased over time (Phase 1-3) (**Figure 9b, 9c)**. This could reflect a gradual rebalancing between flow and metabolism as the brain enters a new neurovascular steady state. These findings are consistent with results from Zhao et al. (Zhao et al. 2025).

The subgenual region is associated with high oxidative metabolism at rest, with elevated baseline $CMRO_2$ and dense microvascularization. Its resting electrophysiology is dominated by theta and alpha rhythms. These properties likely limit the region's ability to sustain prolonged BOLD elevations, while tPBM enhances mitochondrial activity and transiently increases $CMRO_2$, the combination of high baseline metabolic demand and slower oscillatory dynamics resulting in a block-shaped response that peaks and saturates during stimulation, then rapidly declining post stimulation. It is possible that the subgenual region's distinctive structural and functional organization (Palomero-Gallagher et al. 2015), particularly its role as an integrated pathway for regulation (Drevets et al. 2008; Jahn et al. 2010) clears metabolic waste generated during the period of heightened oxidative metabolism, allowing CBF to return to baseline immediately post-stimulus, in contrast to other regions where sustained blood flow persists. These dynamics contrast with the sustained hemodynamic response in Scenario 1. This work highlights how region-specific metabolic and electrophysiological profiles can help to shape the BOLD temporal profile.

Limitations

This study evaluates the immediate short-term effects of 4-minutes of tPBM stimulation. While these acute changes in BOLD and CBF provide insight into the brain's hemodynamic response, it may not reflect long-lasting neuromodulatory changes that could emerge with repeated tPBM stimulations or prolonged light exposure. Data collection was also limited to four minutes of post-stimulation acquisition, preventing characterization of delayed BOLD and CBF responses over a longer period of time. Moreover, CBF measurements have an inherently low signal-to-

bioRxiv preprint doi: https://doi.org/10.1101/2025.11.20.689588; this version posted November 21, 2025. The copyright holder for this preprint (which was not certified by peer review) is the author/funder. All rights reserved. No reuse allowed without permission.

noise ratio, which may have reduced the sensitivity to small or transient changes in perfusion, and without direct metabolic readouts can constrain the physiological interpretation.

Conclusion

This study demonstrates that tPBM can modulate both the BOLD and CBF response, across various cortical structures in the human brain through a single-source laser. Stimulation parameters play a key role in dictating the amplitude of the response as well as the spatial extent. Significant differences within specific significant parameters were seen to vary across brain regions. Regions including the posterior superior temporal gyrus and the posterior cingulate show that 808 nm is more effective at enhancing the BOLD and CBF response compared to structures such as the subgenual which benefits from longer wavelengths, such as 1064 nm. Skin tone modulated the magnitude of the BOLD response, with darker skin causing a reduced response. 10Hz frequency modulated the response in the posterior superior temporal gyrus and the posterior cingulate compared to 40 Hz. To our knowledge, this is the first study to utilize fMRI to determine the effect of the BOLD and CBF response on the various stimulation parameters. Our work has illuminated three main regions of interest that have varying responses to specific parameters. Future work could implement these dosing parameters and provide repeated stimulation to various participant populations.

References

Adebimpe, Azeez, Maxwell Bertolero, Sudipto Dolui, et al. 2022. “ASLPrep: A Platform for Processing of Arterial Spin Labeled MRI and Quantification of Regional Brain Perfusion.” *Nature Methods* 19 (6): 683–686.

Baik, Ji Soo, Tae Young Lee, Nam Gyun Kim, et al. 2021. “Effects of Photobiomodulation on Changes in Cognitive Function and Regional Cerebral Blood Flow in Patients with Mild Cognitive Impairment: A Pilot Uncontrolled Trial.” *Journal of Alzheimer’s Disease: JAD* 83 (4): 1513–1519.

Bandettini, Peter A. 2014. “Neuronal or Hemodynamic? Grappling with the Functional MRI Signal.” *Brain Connectivity* 4 (7): 487–498.

Beckmann, Christian F., and Stephen M. Smith. 2004. “Probabilistic Independent Component Analysis for Functional Magnetic Resonance Imaging.” *IEEE Transactions on Medical Imaging* 23 (2): 137–152.

Cassano, Paolo, Anh Phong Tran, Husam Katnani, et al. 2019. “Selective Photobiomodulation for Emotion Regulation: Model-Based Dosimetry Study.” *Neurophotonics* 6 (1): 015004.

Chan, Agnes S., Tsz-Lok Lee, Michael R. Hamblin, and Mei-Chun Cheung. 2021. “Photobiomodulation Enhances Memory Processing in Older Adults with Mild Cognitive Impairment: A Functional near-Infrared Spectroscopy Study.” *Journal of Alzheimer’s Disease: JAD* 83 (4): 1471–1480.

Chao, Linda L. 2019. “Effects of Home Photobiomodulation Treatments on Cognitive and Behavioral Function, Cerebral Perfusion, and Resting-State Functional Connectivity in Patients with Dementia: A Pilot Trial.” *Photobiomodulation, Photomedicine, and Laser Surgery* 37 (3): 133–141.

Chen, Joanna, Hannah Van Lankveld, Xiaole Z. Zhong, and J. Jean Chen. 2025. “Real-Time Spatial Evolution of the fMRI Response to Photobiomodulation in the Healthy Human Brain.” In *Physiology*, No. Biorxiv;2025.11.17.688884v1. BioRxiv, November 17.

bioRxiv preprint doi: https://doi.org/10.1101/2025.11.20.689588; this version posted November 21, 2025. The copyright holder for this preprint (which was not certified by peer review) is the author/funder. All rights reserved. No reuse allowed without permission.

https://www.biorxiv.org/content/10.1101/2025.11.17.688884v1.

Collman, James P., Abhishek Dey, Richard A. Decreau, et al. 2008. "Interaction of Nitric Oxide with a Functional Model of Cytochrome c Oxidase." *Proceedings of the National Academy of Sciences of the United States of America* 105 (29): 9892–9896.

Cox, R. W. 1996. "AFNI: Software for Analysis and Visualization of Functional Magnetic Resonance Neuroimages." *Computers and Biomedical Research, an International Journal* 29 (3): 162–173.

Davis, T. L., K. K. Kwong, R. M. Weisskoff, and B. R. Rosen. 1998. "Calibrated Functional MRI: Mapping the Dynamics of Oxidative Metabolism." *Proceedings of the National Academy of Sciences of the United States of America* 95 (4): 1834–1839.

Dmochowski, Grzegorz M., Ahmed Duke Shereen, Destiny Berisha, and Jacek P. Dmochowski. 2020. "Near-Infrared Light Increases Functional Connectivity with a Non-Thermal Mechanism." *Cerebral Cortex Communications* 1 (1): tgaa004.

Drevets, Wayne C., Jonathan Savitz, and Michael Trimble. 2008. "The Subgenual Anterior Cingulate Cortex in Mood Disorders." *CNS Spectrums* 13 (8): 663–681.

Ekşi, Murat Şakir, Mustafa Güdük, and Murat Imre Usseli. 2020. "Frontal Bone Is Thicker in Women and Frontal Sinus Is Larger in Men: A Morphometric Analysis." *The Journal of Craniofacial Surgery* Publish Ahead of Print (5). https://doi.org/10.1097/scs.0000000000007256.

El Khoury, Hala, John Mitrofanis, and Luke A. Henderson. 2019. "Exploring the Effects of near Infrared Light on Resting and Evoked Brain Activity in Humans Using Magnetic Resonance Imaging." *Neuroscience* 422 (December): 161–171.

Fischl, Bruce. 2012. "FreeSurfer." *NeuroImage* 62 (2): 774–781.

Foster, Brett L., and Seth R. Koslov. 2025. "Functions of the Posterior Cingulate Cortex and Default Network." *Current Opinion in Behavioral Sciences* 65 (101560): 101560.

Gaggi, Naomi L., Katherine A. Collins, Javier Gonzalez-Castillo, et al. 2024. "Transcranial Photobiomodulation Increases Intrinsic Brain Activity within Irradiated Areas in Early Alzheimer's Disease: Potential Link with Cerebral Metabolism." *Brain Stimulation* 17 (2): 208–210.

Garell, P. C., H. Bakken, J. D. W. Greenlee, et al. 2013. "Functional Connection between Posterior Superior Temporal Gyrus and Ventrolateral Prefrontal Cortex in Human." *Cerebral Cortex (New York, N.Y.: 1991)* 23 (10): 2309–2321.

Gur, R. E., and R. Gur. 1990. "Gender Differences in Regional Cerebral Blood Flow." *Schizophrenia Bulletin* 16 (2): 247–254.

Hamblin, Michael R. 2016. "Shining Light on the Head: Photobiomodulation for Brain Disorders." *BBA Clinical* 6 (December): 113–124.

Hamblin, Michael R. 2018. "Photobiomodulation for Traumatic Brain Injury and Stroke." *Journal of Neuroscience Research* 96 (4): 731–743.

Hare, Hannah V., Nicholas P. Blockley, Alexander G. Gardener, Stuart Clare, and Daniel P. Bulte. 2015. "Investigating the Field-Dependence of the Davis Model: Calibrated fMRI at 1.5, 3 and 7T." *NeuroImage* 112 (May): 189–196.

Hennessy, Madison, and Michael R. Hamblin. 2017. "Photobiomodulation and the Brain: A New

bioRxiv preprint doi: https://doi.org/10.1101/2025.11.20.689588; this version posted November 21, 2025. The copyright holder for this preprint (which was not certified by peer review) is the author/funder. All rights reserved. No reuse allowed without permission.

Paradigm." *Journal of Optics (2010)* 19 (1): 013003.

Hoge, R. D., J. Atkinson, B. Gill, G. R. Crelier, S. Marrett, and G. B. Pike. 1999. "Investigation of BOLD Signal Dependence on Cerebral Blood Flow and Oxygen Consumption: The Deoxyhemoglobin Dilution Model." *Magnetic Resonance in Medicine* 42 (5): 849–863.

Holmes, Emma, Douglas W. Barrett, Celeste L. Saucedo, Patrick O'Connor, Hanli Liu, and F. Gonzalez-Lima. 2019. "Cognitive Enhancement by Transcranial Photobiomodulation Is Associated with Cerebrovascular Oxygenation of the Prefrontal Cortex." *Frontiers in Neuroscience* 13 (October): 1129.

Huang, Ying-Ying, Sulbha K. Sharma, James Carroll, and Michael R. Hamblin. 2011. "Biphasic Dose Response in Low Level Light Therapy - an Update." *Dose-Response: A Publication of International Hormesis Society* 9 (4): 602–618.

Huppert, Theodore J., Solomon G. Diamond, and David A. Boas. 2008. "Direct Estimation of Evoked Hemoglobin Changes by Multimodality Fusion Imaging." *Journal of Biomedical Optics* 13 (5): 054031.

Jahan, Ali, Mohammad Ali Nazari, Javad Mahmoudi, Farzad Salehpour, and Maryam Moghadam Salimi. 2019. "Transcranial near-Infrared Photobiomodulation Could Modulate Brain Electrophysiological Features and Attentional Performance in Healthy Young Adults." *Lasers in Medical Science* 34 (6): 1193–1200.

Jahn, Allison L., Andrew S. Fox, Heather C. Abercrombie, et al. 2010. "Subgenual Prefrontal Cortex Activity Predicts Individual Differences in Hypothalamic-Pituitary-Adrenal Activity across Different Contexts." *Biological Psychiatry* 67 (2): 175–181.

Jenkinson, Mark, Christian F. Beckmann, Timothy E. J. Behrens, Mark W. Woolrich, and Stephen M. Smith. 2012. "FSL." *NeuroImage* 62 (2): 782–790.

Ji, Qipei, Shichang Yan, Jilin Ding, et al. 2023. "Photobiomodulation Improves Depression Symptoms: A Systematic Review and Meta-Analysis of Randomized Controlled Trials." *Frontiers in Psychiatry* 14: 1267415.

Lin, Ai-Ling, Peter T. Fox, Yihong Yang, Hanzhang Lu, Li-Hai Tan, and Jia-Hong Gao. 2008. "Evaluation of MRI Models in the Measurement of CMRO2 and Its Relationship with CBF." *Magnetic Resonance in Medicine* 60 (2): 380–389.

Liu, Careesa C., Sujoy Ghosh Hajra, Teresa P. L. Cheung, Xiaowei Song, and Ryan C. N. D'Arcy. 2017. "Spontaneous Blinks Activate the Precuneus: Characterizing Blink-Related Oscillations Using Magnetoencephalography." *Frontiers in Human Neuroscience* 11 (October): 489.

Liu, Thomas T., and Eric C. Wong. 2005. "A Signal Processing Model for Arterial Spin Labeling Functional MRI." *NeuroImage* 24 (1): 207–215.

Lundqvist, Mikael, Jonas Rose, Pawel Herman, Scott L. Brincat, Timothy J. Buschman, and Earl K. Miller. 2016. "Gamma and Beta Bursts Underlie Working Memory." *Neuron* 90 (1): 152–164.

McCormick, Laurie M., Thoru Yamada, Malcolm Yeh, Michael C. Brumm, and Robert W. Thatcher. 2009. "Antipsychotic Effect of Electroconvulsive Therapy Is Related to Normalization of Subgenual Cingulate Theta Activity in Psychotic Depression." *Journal of Psychiatric Research* 43 (5): 553–560.

Miller, Kathleen B., Anna J. Howery, Leonardo A. Rivera-Rivera, et al. 2019. "Age-Related Reductions in Cerebrovascular Reactivity Using 4D Flow MRI." *Frontiers in Aging*

bioRxiv preprint doi: https://doi.org/10.1101/2025.11.20.689588; this version posted November 21, 2025. The copyright holder for this preprint (which was not certified by peer review) is the author/funder. All rights reserved. No reuse allowed without permission.

Neuroscience 11 (October): 281.

Montazeri, Katayoon, Mohammad Farhadi, Reza Fekrazad, Zeinab Akbarnejad, Samira Chaibakhsh, and Saeid Mahmoudian. 2021. "Transcranial Photobiomodulation in the Management of Brain Disorders." *Journal of Photochemistry and Photobiology. B, Biology* 221 (112207): 112207.

Naeser, Margaret A., Michael D. Ho, Paula I. Martin, Michael R. Hamblin, and Bang-Bon Koo. 2020. "Increased Functional Connectivity within Intrinsic Neural Networks in Chronic Stroke Following Treatment with Red/near-Infrared Transcranial Photobiomodulation: Case Series with Improved Naming in Aphasia." *Photobiomodulation, Photomedicine, and Laser Surgery* 38 (2): 115–131.

Nourski, Kirill V., Mitchell Steinschneider, Ariane E. Rhone, et al. 2021. "Electrophysiology of the Human Superior Temporal Sulcus during Speech Processing." *Cerebral Cortex (New York, N.Y.: 1991)* 31 (2): 1131–1148.

Palomero-Gallagher, Nicola, Simon B. Eickhoff, Felix Hoffstaedter, et al. 2015. "Functional Organization of Human Subgenual Cortical Areas: Relationship between Architectonical Segregation and Connectional Heterogeneity." *NeuroImage* 115 (July): 177–190.

Passow, Susanne, Karsten Specht, Tom Christian Adamsen, et al. 2015. "Default-Mode Network Functional Connectivity Is Closely Related to Metabolic Activity: Metabolic Activity and DMN Connectivity." *Human Brain Mapping* 36 (6): 2027–2038.

Raichle, M. E., A. M. MacLeod, A. Z. Snyder, W. J. Powers, D. A. Gusnard, and G. L. Shulman. 2001. "A Default Mode of Brain Function." *Proceedings of the National Academy of Sciences of the United States of America* 98 (2): 676–682.

Saucedo, Celeste L., Emily C. Courtois, Zachary S. Wade, et al. 2021. "Transcranial Laser Stimulation: Mitochondrial and Cerebrovascular Effects in Younger and Older Healthy Adults." *Brain Stimulation* 14 (2): 440–449.

Setchfield, Kerry, Alistair Gorman, A. Hamish R. W. Simpson, Michael G. Somekh, and Amanda J. Wright. 2024. "Effect of Skin Color on Optical Properties and the Implications for Medical Optical Technologies: A Review." *Journal of Biomedical Optics* 29 (1): 010901.

Thunshelle, Connor, and Michael R. Hamblin. 2016. "Transcranial Low-Level Laser (light) Therapy for Brain Injury." *Photomedicine and Laser Surgery* 34 (12): 587–598.

Tian, Fenghua, Snehal N. Hase, F. Gonzalez-Lima, and Hanli Liu. 2016. "Transcranial Laser Stimulation Improves Human Cerebral Oxygenation: HUMAN CEREBRAL OXYGENATION BY LASER STIMULATION." *Lasers in Surgery and Medicine* 48 (4): 343–349.

Truong, Nghi Cong Dung, Xinlong Wang, Hashini Wanniarachchi, and Hanli Liu. 2022. "Enhancement of Frequency-Specific Hemodynamic Power and Functional Connectivity by Transcranial Photobiomodulation in Healthy Humans." *Frontiers in Neuroscience* 16 (June): 896502.

Urquhart, Elizabeth L., Hashini Wanniarachchi, Xinlong Wang, Francisco Gonzalez-Lima, George Alexandrakis, and Hanli Liu. 2020. "Transcranial Photobiomodulation-Induced Changes in Human Brain Functional Connectivity and Network Metrics Mapped by Whole-Head Functional near-Infrared Spectroscopy in Vivo." *Biomedical Optics Express* 11 (10): 5783–5799.

Van Lankveld, Hannah, Anh Q. Mai, Lew Lim, Nazanin Hosseinkhah, Paolo Cassano, and J. Jean Chen. 2025. "Simulation-Based Dosimetry of Transcranial and Intranasal Photobiomodulation of the Human Brain: The Roles of Wavelength, Power Density, and Skin Tone." *Biomedical Optics*

bioRxiv preprint doi: https://doi.org/10.1101/2025.11.20.689588; this version posted November 21, 2025. The copyright holder for this preprint (which was not certified by peer review) is the author/funder. All rights reserved. No reuse allowed without permission.

Express 16 (8): 3295–3314.

Vink, Jord J. T., Stefano Mandija, Petar I. Petrov, Cornells A. T. van den Berg, Iris E. C. Sommer, and Sebastiaan F. W. Neggers. 2018. "A Novel Concurrent TMS-fMRI Method to Reveal Propagation Patterns of Prefrontal Magnetic Brain Stimulation." *Human Brain Mapping* 39 (11): 4580–4592.

Wang, Xinlong, Fenghua Tian, Divya D. Reddy, et al. 2017. "Up-Regulation of Cerebral Cytochrome-c-Oxidase and Hemodynamics by Transcranial Infrared Laser Stimulation: A Broadband near-Infrared Spectroscopy Study." *Journal of Cerebral Blood Flow and Metabolism: Official Journal of the International Society of Cerebral Blood Flow and Metabolism* 37 (12): 3789–3802.

Wang, Yuguang, Ying-Ying Huang, Yong Wang, Peijun Lyu, and Michael R. Hamblin. 2017. "Photobiomodulation of Human Adipose-Derived Stem Cells Using 810nm and 980nm Lasers Operates via Different Mechanisms of Action." *Biochimica et Biophysica Acta. General Subjects* 1861 (2): 441–449.

Wurtman, R. J. 1975. "The Effects of Light on the Human Body." *Scientific American* 233 (1): 69–77.

Yan, Bingzi, Jie Zhou, Fengshuo Yan, et al. 2025. "Unlocking the Potential of Photobiomodulation Therapy for Brain Neurovascular Coupling: The Biological Effects and Medical Applications." *Journal of Cerebral Blood Flow and Metabolism: Official Journal of the International Society of Cerebral Blood Flow and Metabolism* 45 (5): 800–830.

Yang, Xue, Guangxia Yang, Ruojun Wang, et al. 2023. "Brain Glucose Metabolism on [18F]-FDG PET/CT: A Dynamic Biomarker Predicting Depression and Anxiety in Cancer Patients." *Frontiers in Oncology* 13 (May): 1098943.

Yarkoni, Tal, Russell A. Poldrack, Thomas E. Nichols, David C. Van Essen, and Tor D. Wager. 2011. "Large-Scale Automated Synthesis of Human Functional Neuroimaging Data." *Nature Methods* 8 (8): 665–670.

Yuan, Yaoshen, Paolo Cassano, Matthew Pias, and Qianqian Fang. 2020. "Transcranial Photobiomodulation with near-Infrared Light from Childhood to Elderliness: Simulation of Dosimetry." *Neurophotonics* 7 (1): 015009.

Zein, Randa, Wayne Selting, and Michael R. Hamblin. 2018. "Review of Light Parameters and Photobiomodulation Efficacy: Dive into Complexity." *Journal of Biomedical Optics* 23 (12): 1–17.

Zhang, Q., H. Ma, S. Nioka, and B. Chance. 2000. "Study of near Infrared Technology for Intracranial Hematoma Detection." *Journal of Biomedical Optics* 5 (2): 206–213.

Zhang, Zhixin, Zhiyu Zhang, Peng Liu, et al. 2024. "The Role of Photobiomodulation to Modulate Ion Channels in the Nervous System: A Systematic Review." *Cellular and Molecular Neurobiology* 44 (1): 79.

Zhao, Chenguang, Zhilin Li, Zhaohuan Ding, et al. 2025. "Effect of Transcranial Light Stimulation on the Neurovascular Unit in the Human Brain." In *bioRxiv*. April 26. https://doi.org/10.1101/2025.04.23.649937.

Zupin, Luisa, Alessandra Gianoncelli, Fulvio Celsi, et al. 2024. "The Effect of near-Infrared Photobiomodulation Therapy on the Ion Content of 50B11 Sensory Neurons Measured through XRF Analysis." *Journal of Photochemistry and Photobiology. B, Biology* 259 (113019): 113019.